frontiers | Frontiers in Remote Sensing

ORIGINAL RESEARCH
published: 02 May 2022
doi: 10.3389/frsen.2022.777314

Reduction of Spectral Radiance Reflectance During the Annular Solar Eclipse of 21 June 2020 Observed by EPIC

Guoyong Wen[1,2]*, *Alexander Marshak*[1], *Jay Herman*[1,3] *and Dong Wu*[1]

[1]NASA Goddard Space Flight Center, Greenbelt, MD, United States, [2]Goddard Earth Sciences Technology Research, Morgan State University, Baltimore, MD, United States, [3]Joint Center for Earth Systems Technology, University of Maryland Baltimore County, Baltimore, MD, United States

The annular solar eclipse on 21 June 2020 passed over desert areas (parts of Central and Eastern Africa, the southern Arabian Peninsula), partly cloudy regions (parts of South Asia and the Himalayas), and the mostly cloudy region in East Asia. Moving around the Earth-Sun Lagrange point 1 (L_1), the Earth Polychromatic Imaging Camera (EPIC) instrument on the Deep Space Climate Observatory (DSCOVR) spacecraft captured three sets of images of the sunlit Earth during the eclipse, allowing us to study the impact of the solar eclipse on reflected solar radiation when the underlying surface and/or cloudy conditions in the Moon's shadow are quite different. We analyzed EPIC images acquired during the 21 June 2020 and 21 August 2017 eclipses. We found that (1) EPIC-observed average spectral as well as spectrally averaged reflectance reductions of the entire sunlit Earth during the 21 June 2020 solar eclipse are distinctly different from those during the total solar eclipse of 21 August 2017; (2) the reduction of spectral reflectance depends strongly on underlying reflector properties, including the brightness, the area coverage of each reflector in the penumbra and the average distance to the center of the Moon's shadow.

Keywords: eclipse, DSCOVR/EPIC, solar radiation, cloud, surface

OPEN ACCESS

Edited by:
Hartmut Boesch,
University of Leicester,
United Kingdom

Reviewed by:
Yolanda Shea,
Langley Research Center,
United States
Xiuqing Hu,
China Meteorological Administration,
China

***Correspondence:**
Guoyong Wen
Guoyong.Wen@nasa.gov

Specialty section:
This article was submitted to
Satellite Missions,
a section of the journal
Frontiers in Remote Sensing

Received: *15 September 2021*
Accepted: *08 April 2022*
Published: *02 May 2022*

Citation:
Wen G, Marshak A, Herman J and Wu D (2022) Reduction of Spectral Radiance Reflectance During the Annular Solar Eclipse of 21 June 2020 Observed by EPIC.
Front. Remote Sens. 3:777314.
doi: 10.3389/frsen.2022.777314

INTRODUCTION

A rare but spectacular event in the Sun-Earth-Moon system, a solar eclipse occurs when the Moon moves between the Sun and Earth, casting a shadow on Earth and resulting in the reduction of the incident solar irradiance at the top-of-atmosphere (TOA). The Moon's shadow consists of two parts: umbra and penumbra. The umbra is the Moon's dark inner shadow, from where total solar eclipse is visible; the penumbra is the Moon's faint outer shadow, from where partial solar eclipses are visible. Typically, the umbra is 100–160 km wide, while the penumbra diameter can be greater than 6,400 km. Thus, a solar eclipse has a strong impact on local solar radiation budget, particularly in and near umbra regions, and significant impact on global average solar radiation budget.

Over the past several decades, researchers have studied the impact of an eclipse on surface solar radiation from ground-based radiometer observations and radiative transfer simulations. Several ground-based radiation experiments and modeling activities have been carried out to understand radiation in solar eclipse conditions in the past. Sharp et al. (1971) reported that the sky light may be considered as attenuated sunlight up to at least 99.8% obscuration and the effect of multiple scattering from outside the umbral region dominates the sky brightness close to and during totality

(e.g., Mikhalev et al., 1999; Zerefos et al., 2000). Shaw (1978) developed a model to compute sky radiance during a total solar eclipse by including first- and second-order scattering processes that would compute the diffused light scattered into the umbra. Koepke et al. (2001) studied surface spectral variation of the solar radiation during an eclipse, and Emde and Mayer (2007) performed a full 3D radiative transfer simulation of surface spectral solar radiance and irradiance change for cloudless atmosphere during a total eclipse on 29 March 2006, providing a benchmark for studying radiative transfer under solar eclipse conditions.

During the recent total eclipse on 21 August 2017, Bernhard and Petkov (2019) made surface spectral solar irradiance observations and performed 3D radiative transfer simulations; Ockenfuβ et al. (2020) further used 3D radiative transfer simulations for understanding the impact of surface spectral albedo, ozone vertical distribution and surrounding mountains on surface spectral irradiance observed by Bernhard and Petkov (2019); Wen et al. (2020) used ground-based pyranometer observations to estimate the impact of solar eclipse on surface broadband irradiance reduction; Calamas et al. (2018) studied the impact of the eclipse on surface irradiance and ambient temperature; and Eshelman et al. (2020) studied impact of total solar eclipse on all-sky polarization images. Gedzelman (2020) showed that the sunlit tops of cloud layers and arctic sea ice near the umbra appeared salmon-brown when viewed from airplanes or satellite during the 21 August 2017 as well as 2 July 2019 eclipse. Sarid et al. (2021) demonstrated the radiance reduction observed by Terra MODIS for several eclipse events. Madhavan and Venkat Ratnam (2021) studied the impact of a solar eclipse on surface radiation and photovoltaic energy.

One major impact of a solar eclipse is the reduction of the TOA input solar radiation, resulting in global and local reduction in incident and reflected solar radiation. Although the distribution of incoming solar radiation can be calculated with high accuracy, the global reduction of reflected solar radiation remained unknown until the 2015 launch of the Deep Space Climate Observatory (DSCOVR) satellite. For the first time, Herman et al. (2018a) used observations from the Earth Polychromatic Imaging Camera (EPIC) instrument to estimate the average reflectance reduction of the sunlit Earth disk. Flying onboard the DSCOVR satellite located near the Earth-Sun Lagrange point 1 (L_1), about 1.5 million kilometers from the Earth and with a spacecraft-Earth-Sun angle varying from 2° to 12° (Marshak et al., 2018; Marshak et al., 2021), the EPIC instrument views the entire sunlit side of the Earth including the shadow of the Moon during a solar eclipse. Herman et al. (2018a) showed that the day-to-day variability of the disk average reflectance from EPIC image at similar UTC times is very small. Thus, the EPIC images taken at a similar UTC time from the day before or after can be used as a reference to estimate the eclipse-induced disk reflectance reduction.

Evidence shows that the brighter the atmosphere-surface under the Moon's shadow, the larger the solar eclipse impact on the reflected solar radiation. Since the TOA reflectance depends on wavelength and underlying surface type and cloud amount, it is necessary to study the eclipse induced reflectance when the Moon's shadow is over different atmosphere-surface conditions.

In this study, we use three sets of EPIC images acquired during the 21 June 2020 annular eclipse when the center of the Moon's shadow was in the Arabian Peninsula, Himalayas, and Southwest China to quantify and understand the impact of the eclipse on the average reflectance reduction over the sunlit disk. We further compare the reflectance reductions during the 2020 eclipse with two sets of EPIC images acquired during the 2017 Great American eclipse over Casper, Wyoming and Columbia, Missouri where the surface reflective properties and cloud fraction differ significantly. In **Section 2**, we describe the EPIC data and methodology used in this study. The results are presented in **Section 3** followed by the summary in **Section 4**.

DATA AND METHODS

We use EPIC observations to estimate the reduction of spectral solar irradiances during solar eclipses. EPIC is a 10-channel spectroradiometer onboard the DSCOVR spacecraft flying in a Lissajous orbit around the L_1 point, where the combined gravitational pull of the Sun and Earth equals the centripetal force required for the spacecraft to move with them. The DSCOVR orbit has a period of 6 months, resulting in a spacecraft-Earth-Sun angle varying from 2° to 12°. This allows EPIC to view the Moon's shadow in the sunlit disk of the Earth under eclipse conditions. EPIC consists of a 30-cm aperture Cassegrain telescope with a 0.62° field of view (FOV) encompassing the Earth that has a nominal size of 0.5° at the L_1 point. EPIC provides 10 narrowband spectral images of the entire sunlit side of Earth using a 2048 × 2048 pixel charge-coupled device (CCD) detector every 65 min (in the Northern Hemisphere summer) to 111 min (in the Northern Hemisphere winter). The wavelengths range from ultraviolet (UV), to visible, to near infrared (NIR). The sampling size on the Earth is nominally ~8 × 8 km^2 at the center of the image with an effective spatial resolution of 12 × 12 km^2 for the 443 nm channel when EPIC's point spread function is considered. To reduce the downlink transmission time, the images for all wavelengths, except 443 nm, have been reduced to 1,024 × 1,024 pixels. A more detailed description of EPIC is given in Herman et al. (2018b) and Marshak et al. (2018).

In this study, we use EPIC level 1B (L1B) version 3 data distributed by the Atmospheric Science Data Center of NASA Langley Research Center (https://eosweb.larc.nasa.gov). The L1B digital counts multiplied by the after-launch wavelength dependent calibration coefficient (Geogdzhayev and Marshak, 2018; Herman et al., 2018b; Doelling et al., 2019; Geogdzhaev et al., 2021) yield TOA reflectance. While the EPIC images are geolocation processed (Blank et al., 2021), the L1B algorithm produces images in which all wavelengths are regridded to the same common grid, i.e., every pixel has the same geolocation (latitude and longitude) for all 10 wavelength channels.

Three sets of images were acquired by EPIC on 21 June 2020 when the center of the Moon's shadow eclipse was in the Arabian Peninsula, Himalayas, and East Asia (Southwest of China). The

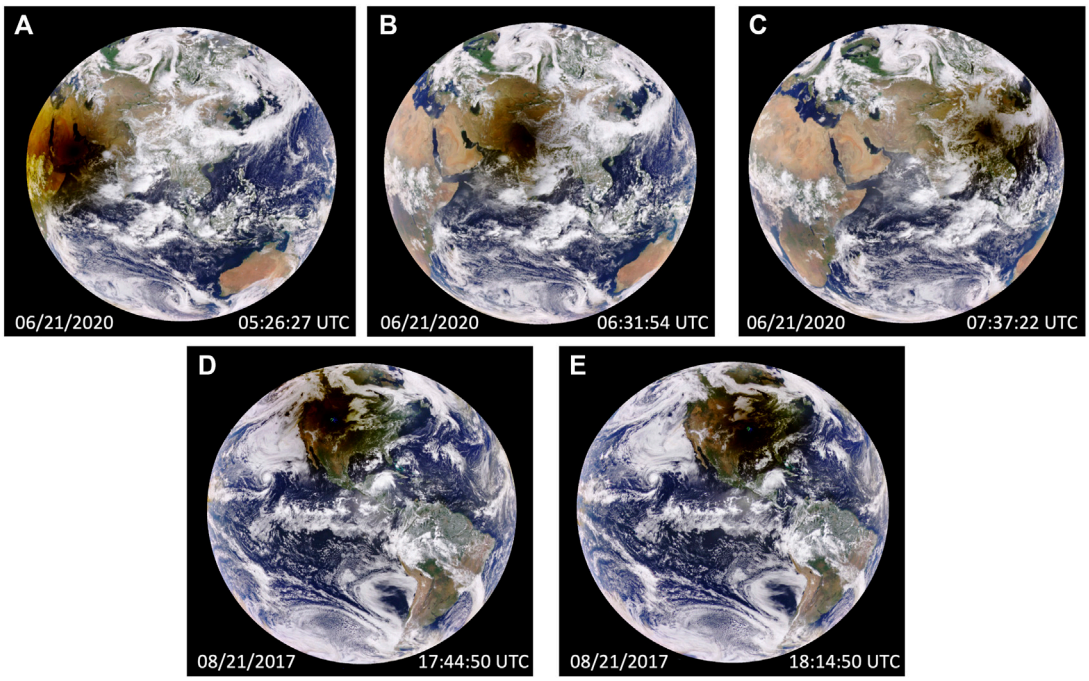

FIGURE 1 | Three EPIC images taken during 21 June 2020 solar eclipse when the center of the Moon's shadow was in **(A)** Arabian Peninsula, **(B)** Himalayas, and **(C)** Southwest China. Two EPIC images taken during 21 August 2017 when the center of the Moon's shadow was in **(D)** Casper, Wyoming and **(E)** Columbia, Missouri.

TABLE 1 | Eclipse measurement time and location of the center of the Moon's shadow of five sets of EPIC images.

	YY/MM/DD	UTC	Latitude	Longitude
Casper, WY	2017/08/21	17:44:50	42.8666°N	106.3131°W
Columbia, MO	2017/08/21	17:54:36	38.9517°N	92.3341°W
Arabian Peninsula	2020/06/21	05:26:27	20.5115°N	53.7671°E
Himalayas	2020/06/21	06:31:54	30.0267°N	76.9467°E
Southwest China	2020/06/21	07:37:22	29.7300°N	101.1630°E

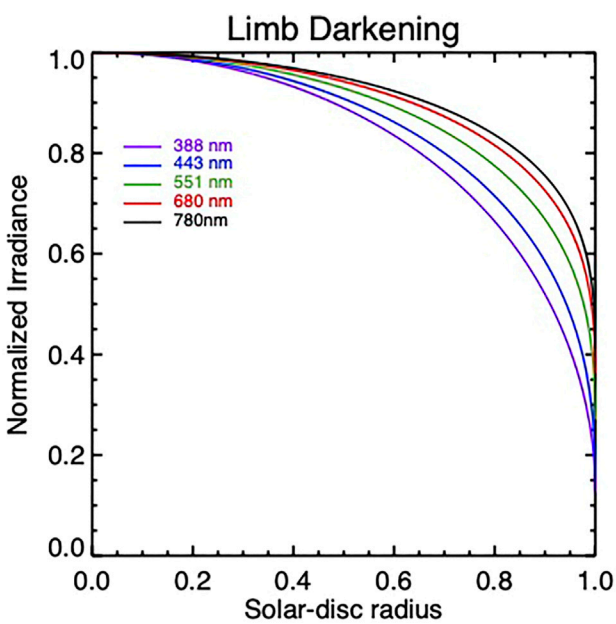

FIGURE 2 | Limb darkening function based on Neckel (2005).

surface and/or cloudy conditions in the Moon's shadow are quite different. The Arabian Peninsula is a vast desert wilderness in Western Asia; the Himalayas are a mountain range in South and East Asia; and most of the surface in Southwest China is covered by vegetation. Most of the Arabian Peninsula was cloud free; the Himalayas were mostly; and Southwest China was mostly cloudy. Two sets of images were taken by EPIC during the 2017 eclipse when the totality was in Casper, Wyoming and Columbia, Missouri. The surrounding areas of the Casper site are mostly covered by grasslands; while the surrounding areas of the Columbia site are mostly covered by croplands. EPIC images during the 21 June 2020 and 21 August 2017 solar eclipses are presented in **Figure 1**. Information about EPIC images acquired during the two eclipses are described in **Table 1**. In this study, we analyze images at five nonabsorbing wavelengths at 388, 443, 551, 680, and 780 nm.

To understand the average reflectance reduction over the sunlit disk we need to quantify the contribution of different reflectors to the average reflectance reduction. Thus, we need to recover the image under hypothetical non-eclipse conditions from the image acquired during the eclipse. Initially, one needs to know the true input spectral solar irradiance for each EPIC image pixel when the part of the solar disk is covered by the Moon.

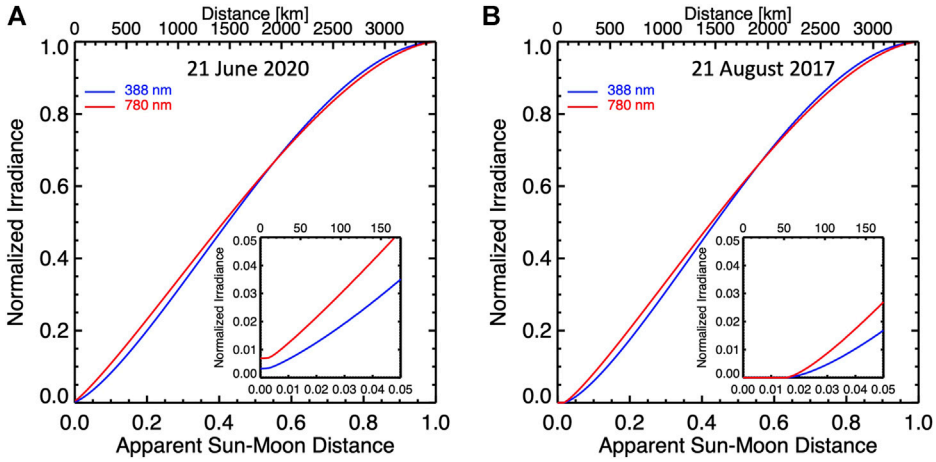

FIGURE 3 | (A) Normalized solar irradiance as a function of apparent Sun-Moon distance in lower X-axis and the distance to the center of the Moon's shadow in upper X-axis on the Earth for the 21 June 2020 eclipse; **(B)** similar to **(A)** but for the 21 August 2017 eclipse. The insets show details of the irradiance variation near the center of the eclipse.

We know the brightness of the Sun's disk decreases from its center to its edge, i.e., limb darkening. Here, we use the limb darkening function from Neckel (2005) based on McMath Solar Telescope and the large vertical spectrograph observations at the National Solar Observatory on Kitt Peak (Neckel and Labs, 1994) to compute the normalized solar irradiance relative to the irradiance at the center of the solar disk as a function of the radius of the Sun (**Figure 2**). Then, we follow Koepke et al. (2001) to compute the brightness of the Sun as a function of apparent Moon-Sun distance X, where X = 0 when the centers of the Moon and the Sun coincide, $X = 1$ when the Moon first contacts the Sun, $X = -1$ when the disk of the Moon leaves the Sun again. On the reference plane passing through the center of the Moon's shadow on Earth and perpendicular to the incident sunlight at a given time, the distance between a point to the center of the Moon's shadow (upper scale of **Figure 3**) is linearly related to X as demonstrated by Emde and Mayer (2007). Thus, one can calculate the normalized solar irradiance during an eclipse, defined as the TOA spectral solar irradiance for solar disk covered by the Moon normalized by the irradiance of the uncovered solar disk, as a function of the Sun-Moon distance (Koepke et al., 2001) or a function of the distance from the center of the Moon's shadow on the reference plane (**Figure 3**). The reference plane almost coincides with the EPIC image plane that is perpendicular to Earth-spacecraft direction since the DSCOVR spacecraft is slightly off the Sun-Moon-Earth line during an eclipse (about 3° for the 21 June 2020 and 7.7° for the 21 August 2017).

Note the difference between the two normalized irradiances in **Figure 3**, due to different eclipse magnitudes of the two eclipses. Although the apparent sizes of the Sun and Moon as viewed from Earth are both about 0.5°, both vary because the Earth-Moon and Earth-Sun distances vary. The angular diameter of the Moon is about 3.1% larger than that of the Sun during the 21 August 2017 total eclipse, while the angular diameter of the Moon is about 0.6% smaller than that of the Sun during the 21 June 2020 annular eclipse. Thus, the normalized irradiances are greater than zero when the Sun and Moon coincide with apparent Sun-Moon distance of zero for the 2020 eclipse.

The distance between a pixel to the center of the Moon's shadow can be estimated in an EPIC image. First, we need to estimate the pixel size in EPIC images. These are projections of the sunlit face of the Earth onto the focal plane of the 2048 × 2048 CCD array. With a 20-km altitude of atmosphere at the edge of the Earth, the Earth's disk diameter in EPIC images is 12,782 km. The pixel size of an EPIC image is estimated by dividing the disk diameter by number of pixels across the diameter in the image. Second, the center of the Moon's shadow changes a little from one image to another because the images are taken at slightly different times. We use the locations (latitude and longitude) of the center of Moon's shadow at specific times as the first estimates (**Table 1**). Then, we search the images around the estimated locations to find the minimum value of reflectance to locate the center of the Moon's shadow for each image. With both pixel size and the center of the Moon's shadow available, the distance between a pixel in the penumbra and the center of the Moon's shadow can be easily calculated. The distance is further multiplied by cosine of Sun-Earth-Vehicle (SEV) angle (Vehicle refers here to the DSCOVR spacecraft) to obtain the corresponding distance in the reference plane from which we calculate the normalized solar irradiance (**Figure 3**) for estimating the reflectance of the pixel under non-eclipse conditions as explained in the following paragraph. The SEV angle for each EPIC image is available at the DSCOVR/EPIC website (https://epic.gsfc.nasa.gov).

Within the Moon's shadow, the digital counts multiplied by the calibration coefficient yields apparent reflectance ($R_{e,\lambda}$, e stands for eclipse and λ for wavelength)

$$R_{e,\lambda}(i,j) = \frac{\pi I_{\lambda}(i,j)}{I_{0,\lambda}}, \tag{1a}$$

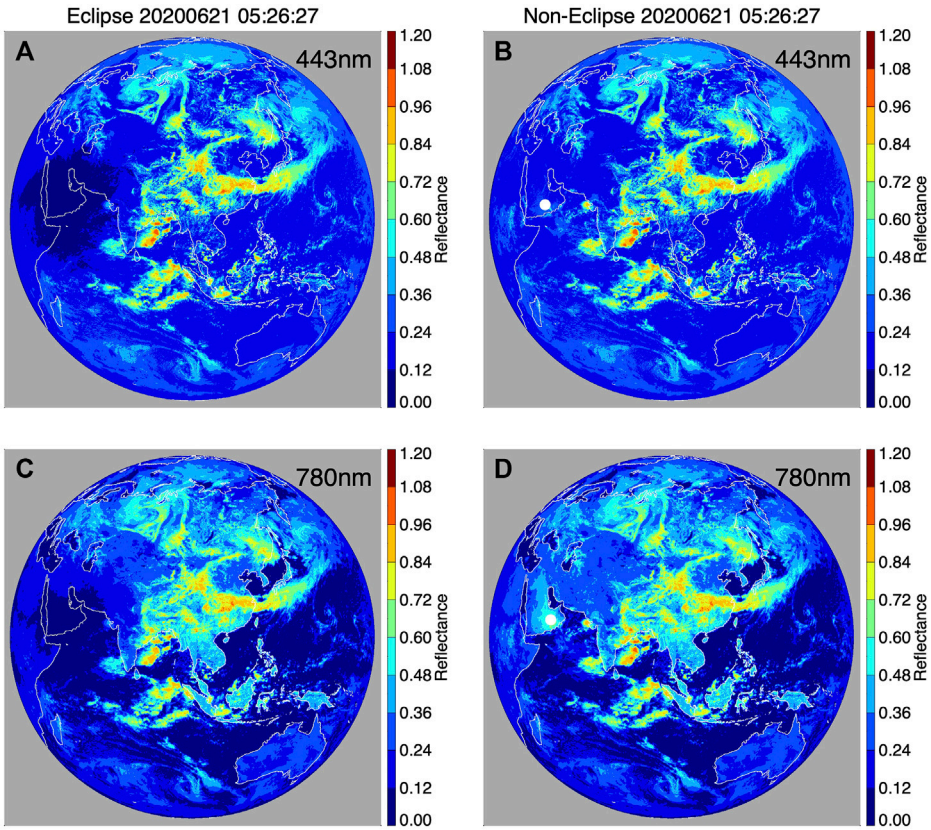

FIGURE 4 | (A) EPIC image at 443 nm acquired during the 21 June 2020 eclipse when the center of the Moon's shadow was in Arabian Peninsula; **(B)** the recovered image for hypothetical non-eclipse conditions for image in **(A)**; **(C)** similar to **(A)** but for 780 nm; **(D)** similar to **(B)** but for 780 nm. The white circles in **(B)** and **(D)** are the center of the Moon's shadow with a radius of about 170 km.

where $I_\lambda(i, j)$ is the reflected radiance of pixel (i, j), $I_{0,\lambda}$ is the incident spectral solar irradiance at wavelength λ for normal conditions (or uncovered solar disk). For the same TOA reflected radiance $I_\lambda(i, j)$, the true reflectance ($R_{ne,\lambda}$, *ne* stands for non-eclipse) is

$$R_{ne,\lambda}(i, j) = \frac{\pi I_\lambda(i, j)}{I'_{0,\lambda}(i, j)}, \tag{1b}$$

where $I'_{0,\lambda}(i, j)$ is the incident spectral solar irradiance when the solar disk is partially covered by the Moon. Thus, the reflectance for a hypothetical non-eclipse condition can be recovered using the relationship

$$R_{ne,\lambda}(i, j) \approx \frac{R_{e,\lambda}(i, j)}{I_{norm,\lambda}(i, j)} \tag{1c}$$

and

$$I_{norm,\lambda}(i, j) \approx \frac{I'_{0,\lambda}(i, j)}{I_{0,\lambda}} \tag{1d}$$

where $I_{norm,\lambda}(i, j)$ is the normalized irradiance (**Figure 3**) for pixel (i, j) in an EPIC image. Koepke et al. (2001) used this method to compute photolysis frequencies while Trees et al. (2021) applied it to estimate UV absorbing aerosol index for hypothetical non-eclipse conditions.

Examples of the original and recovered images for the 2020 eclipse in the Arabian Peninsula and the 2017 eclipse in Casper, Wyoming are presented in **Figures 4**, **5**, respectively. $I_{norm,\lambda}$ is very small near the center of the Moon's shadow and $I_{norm,\lambda} = 0$ for pixels in the totality. The radiation in this area is strongly influenced by the 3D radiative effects (Emde and Mayer, 2007). The reflectance cannot be calculated using the simple relationship of **Eq.1c**. Here, we neglect the area within a radius of ~170 km from the center of the shadow for both eclipse and corresponding non-eclipse images in computing eclipse-induced reflectance reduction. Since the area neglected is ~0.3% of the total area penumbra of ~3,000 km in radius (see **Figure 3**), neglecting this small area would introduce a negligible error, slightly underestimating the disk-averaged reflectance reduction. Using the normalized TOA solar irradiance, typical disk-averaged spectral reflectance, and reflectance for different reflector types for the center of the Moon's shadow, we found that the errors in reflectance reduction due to neglecting the small area are very small, depending on underlying reflector conditions of the area. For wavelengths from 388 to 780 nm, the error in the reflectance reduction estimate ranges from −0.5% to −0.1% for clear ocean;

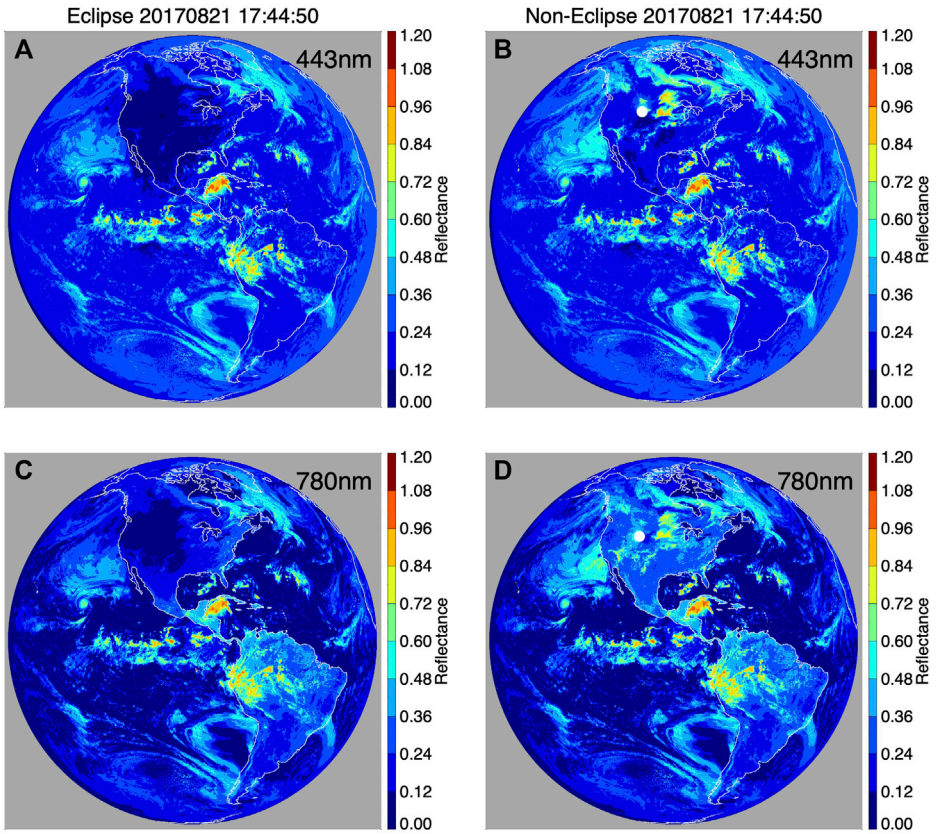

FIGURE 5 | Similar to **Figure 4** but for the 21 August 2017 solar eclipse when the center of the Moon's shadow was in Casper, Wyoming.

−0.6% to −0.8% for clear land; −0.5% to −1.6% for clear vegetation; −1.5% to −1.6% for cloudy ocean; −1.5% to −1.8% for cloudy land; and −1.5 to −2.0% for cloudy vegetation.

From its center, the Moon's shadow can extend large distances (~3,000 km in radius). For that scale, both surface albedo and cloud cover can vary significantly. Thus, to understand the impact of a solar eclipse on the disk average reflectance, one needs to quantify the reflectance reduction from different reflector types. With the recovered image for non-eclipse conditions, we further apply Earth Reflector Type Index (ERTI) developed by Song et al. (2018) for classifying EPIC pixels into four dominant reflector types: clear ocean, clear land, clear green vegetation, and cloud. This method was used to study the blue and near-IR global spectral reflectance relationship as well as the response of global average reflectance to the change in cloud cover from EPIC observations (Wen et al., 2019). We do not separate clouds over land from clouds over ocean, though there are some differences in spectral reflectance between the two types of cloud. On average, cloud is the brightest of all wavelengths among the four dominant reflectors. Thus, dividing the image into four reflector types is sufficient for this study.

An important point is that the ERTI is sensitive to the presence of green leaves in a pixel and attributes the pixel to vegetation if the leaf area index (LAI) is larger than ~0.5 (Song et al., 2018). The area of green leaves can exhibit strong seasonal variation

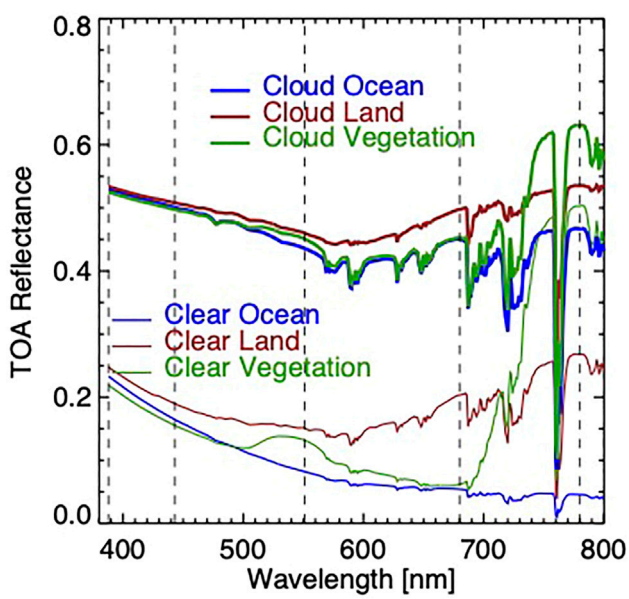

FIGURE 6 | TOA spectral reflectance simulated using SBDART (Ricchiazzi et al., 1998) for clear and cloudy atmospheric conditions over ocean, land, and vegetation. The cloud optical depth is 10, and solar zenith angle is 30°. The vertical dashed lines indicate the EPIC wavelengths.

from its maximum to a very low value (Samanta et al., 2012); therefore, one should distinguish between vegetated land according to a land cover classification map and actual presence of green leaves in the scene. For example, the ERTI classifies savannas in the southern part of Africa as vegetated land during wet season (mean LAI~2.4 in March), and it attributes this land cover type as bare land during dry season (LAI can drop to ~0.4 in August). We emphasize that the clear vegetation refers to cloud-free green vegetation, clear land includes dry vegetation and bare soil. In this study, we do not distinguish clouds over different surface types since the wavelength dependence of reflectance of cloud over ocean is similar to that over land (**Figure 6**). Though the reflectance from clouds over green vegetation has a very different wavelength-dependent signature, the coverage of green vegetation is quite small, less than 5% coverage of any EPIC images (Wen et al., 2019).

RESULTS

Recovering EPIC images for non-eclipse conditions is critical for understanding the reduction of spectral reflectance during a solar eclipse. **Figures 4**, **5** present original and recovered images for the blue-band at 443 nm and the near-IR band at 780 nm for the Arabian Peninsula and Casper, Wyoming during the 2020 and 2017 solar eclipses, respectively. Since both land surface and ocean are dark at 443 nm, the blue-band image can be used to examine the recovered cloud structure. For the Arabian Peninsula case, the clouds that were not visible in the eclipse image (Sudanian savanna to the west of the center of the Moon's shadow) or less bright (to the east and southeast of the center of the Moon's shadow) (**Figure 4A**) become visible and evidently brighter after the correction (**Figure 4B**). Comparing the recovered non-eclipse image with the RGB composite image (**Figure 1A**), we can see that the non-eclipse image has indeed recovered cloud features and enhanced the cloud visibility.

Since land surfaces are bright at 780 nm, the non-eclipse image can be used to examine the recovery of land surface as well as clouds. Under eclipse conditions, the entire Arabian Peninsula and the Sahara Desert in North Africa and part of West Asia were under the Moon's shadow, thereby dark or even invisible in 780 nm image (**Figure 4C**). After the corrections, the Arabian Peninsula is clearly recovered, the Sahara Desert in North Africa and West Asia are recovered, and the coastlines and water bodies next to land (e.g., the Red Sea, the Persian Gulf, the Gulf of Oman, the Arabian Sea, and the Indian Ocean) are clearly visible in the non-eclipse image (**Figure 4D**). Similar to the blue-band, cloud structure in the near-IR image has been recovered or enhanced. Again, one can compare the non-eclipse image with the RGB composite image (**Figure 1A**) to see the recovery of land.

The original eclipse and non-eclipse images during the 2017 solar eclipse over Casper, Wyoming show the recovery of clouds and land after the corrections (**Figure 5**). It is interesting to see the cloud deck off the coast of California and the clouds in North America are much brighter in the non-eclipse images at both 443 and 780 nm bands (**Figures 5B,D**) compared to the eclipse images (**Figures 5A,C**). Clouds to the east of Casper that not clearly visible in the eclipse image are evidently recovered after the correction. In addition to clouds, the land of all North America is brighter at 780 nm in the corrected image compared to the original image.

With both eclipse and non-eclipse images, we estimate the eclipse-induced global reflectance reduction. The global average reflectance can be expressed as a sum of reflectance from each reflector component. Assuming there are N pixels and N_1, N_2, N_3, . . . pixels for type *1*, *2*, *3*, . . . reflector component ($N = \sum_i N_i$) in the whole EPIC image, then the global average reflectance can be expressed as

$$\langle R \rangle = \frac{1}{N}\left[\sum_{i=1}^{N_1} R_1(i) + \sum_{i=1}^{N_2} R_2(i) + \sum_{i=1}^{N_3} R_3(i) + \ldots\right] \quad (2a)$$

where $R_j(i)$ is the reflectance of reflector type j at pixel i (the wavelength dependence is omitted for simplicity). The global reflectance reduction is the difference between the reflectance for non-eclipse $\langle R_{ne} \rangle$ and eclipse conditions $\langle R_e \rangle$

$$\Delta \mathrm{R} = \langle R_{ne} \rangle - \langle R_e \rangle = \sum_j \Delta R_j, \quad (2b)$$

where ΔR_j is the reflectance reduction from j^{th} reflector. We consider pixels in the Moon's shadow only because there is no reflectance reduction outside of the shadow. For j^{th} reflector with n_j pixels in the Moon's shadow in an EPIC image ($n_j < N_j$), the reflectance reduction is

$$\Delta \mathrm{R}_j = \frac{1}{N}\sum_{i=1}^{n_j}\left(R_{ne,j}(i) - R_{e,j}(i)\right). \quad (2c)$$

or

$$\Delta \mathrm{R}_j = \frac{1}{N}\sum_{i=1}^{n_j}\left(1 - I_{norm,j}(i)\right)R_{ne,j}(i) \quad (2d)$$

or

$$\Delta \mathrm{R}_j = \eta_j \frac{\sum_{i=1}^{n_j} R_{ne,j}(i)}{n_j} = \eta_j \bar{R}_{ne,j} \quad (2e)$$

where $\eta_j = \frac{n_j}{N}(1 - \bar{I}_{norm,j})$ and $\bar{I}_{norm,j}$ is the mean value of the normalized solar irradiance for all j^{th} reflector pixels. Thus, the reduction from j^{th} reflector depends on three competing factors, i.e. the average reflectance ($\bar{R}_{ne,j}$), the number of pixels (n_j) in the Moon's shadow or the ratio ($\frac{n_j}{N}$), and average normalized solar irradiance ($\bar{I}_{norm,j}$) of jth reflector in the Moon's shadow. Radiative transfer model-simulated TOA reflectances for clear and cloudy atmospheric conditions over different surface types are presented in **Figure 6** for interpreting observed reflectance reduction.

The average reflectance ($\bar{R}_{ne,j}$) determines the brightness of the reflector. The brighter the reflector, the larger the associated reduction. The more pixels in the Moon's shadow, the larger the ratio $\frac{n_j}{N}$, the larger the reduction. $\bar{I}_{norm,j}$ is a measure of the average radial distance of the pixels to the center of the Moon's shadow. Near the center of the Moon's shadow, $\bar{I}_{norm,j}$ is small and $1 - \bar{I}_{norm,j}$ is large, resulting in large reflectance reduction; conversely, far from the center of the Moon's shadow, $\bar{I}_{norm,j}$ approaches 1 and η_j

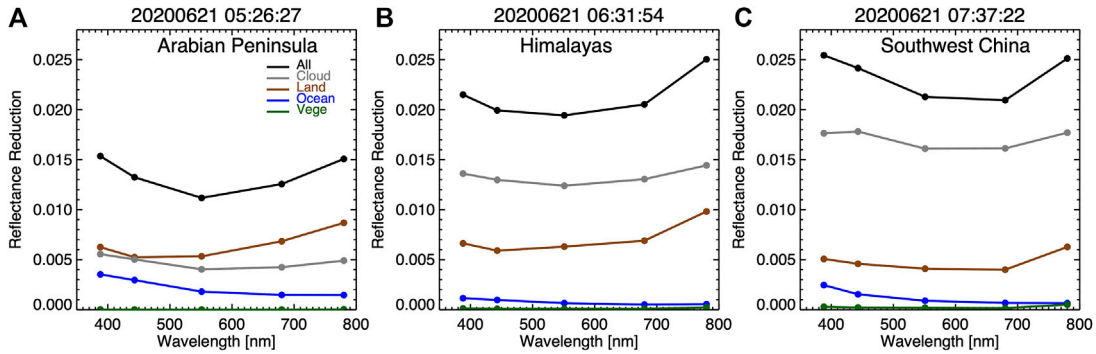

FIGURE 7 | Disk average reflectance reduction with contributions from different reflector types for the 2020 solar eclipse when the center of the Moon's shadow was in **(A)** Arabian Peninsula, **(B)** Himalayas, **(C)** Southwest China.

approaches 0, resulting in small reflectance reduction. Thus, the reflectance reduction from j^{th} reflector is proportional to the average reflectance of the reflector within the Moon's shadow. However, the associated reflectance reduction (ΔR_j) can be very small if the number of pixels is nominal or the pixels are near the edges of the Moon's shadow ($\bar{I}_{norm,j}$ approaches 1) even if the reflector is very bright. We call η_j the contribution factor that accounts for the effects of both number of pixels in the Moon's shadow and average distance of pixels to the center of the Moon's shadow for j^{th} reflector.

Figure 7 shows the disk average spectral reflectance reduction and associated contribution from different reflector types when the center of the 21 June 2020 solar eclipse was in the Arabian Peninsula, the Himalayas, and Southwest China, respectively. For the Arabian Peninsula case (**Figure 7A**), the total disk reflectance reduction decreases from 388 to 551 nm followed by an increase to 780 nm. This feature is explained by the contribution from each reflector type. The land makes the largest contribution to the total reflectance reduction, followed by cloud and then ocean. Green vegetation makes little contribution to the disk average reflectance reduction.

For the Himalayas case (**Figure 7B**), there is a small decrease in the average reflectance reduction from 388 to 551 nm followed by a larger increase in the reduction from 551 to 780 nm compared to the Arabian Peninsula case. Here, clouds make the largest contribution, about two thirds, to the disk average reflectance reduction. Land is the second largest contributor, and, though it is small, clear ocean contributes significantly at shorter wavelengths, and the associated reduction decreases rather quickly with wavelength. Again, green vegetation makes a minimal contribution to the average reflectance reduction.

For the Southwest China case (**Figure 7C**), the total reduction decreases with wavelength from 388 to 551 nm followed by a small decrease from 551 to 680 nm and a large increase from 680 to 780 nm. It is evident that clouds contribute the most, more than 70%, of the total reflectance reduction because a large area near the center of the Moon's shadow is cloudy. Clear land contribution makes the second largest contribution to the total reflectance reduction since the clear land is less reflective than cloud over land and the clear land pixels being farther from the center of the Moon's shadow contribute to the reflectance reduction. Clear ocean makes a significant contribution to the reflectance reduction. In all three 2020 eclipse cases, the contributions from green vegetation are small. The contribution from different reflector types explains the global reflectance reduction for three cases of EPIC-observed global reflectance reductions.

To interpret the reduction from each reflector, we present $\bar{R}_{ne,j}$, $1-\bar{I}_{norm,j}$, and $\frac{n_j}{N}$ (see **Eq.2e**) for each reflector in **Figure 8**. First, we examine the average reflectance of each reflector for the three cases from 2020. It is clear that the reflectance reduction for each reflector (**Figure 7**) is proportional to the average reflectance in the Moon's shadow (**Figures 8a1–a3**). The spectral dependence of EPIC-observed average spectral reflectances are similar to the model simulations (**Figure 6**). For all three cases, on average, cloud is the brightest reflector followed by land. Additionally, green vegetation compared to ocean is darker in UV and blue channels at 388 and 443 nm, similar in visible channels at 551 and 680 nm, and much brighter at near-IR channel at 780 nm. The observed reflectance has large variability for clouds and less variable for clear land, clear ocean, and green vegetations reflectors. The average cloud reflectances for the Himalayas and Southwest China cases are larger than the Arabian Peninsula case: clouds for the Himalayas and Southwest China cases are mostly over land compared to a large fraction of clouds over the Indian Ocean for the Arabian Peninsula case, and, on average, optical depth of water cloud over land is significantly thicker than clouds over ocean while ice clouds over land and ocean have similar optical depth (King et al., 2013). In addition, land is brighter than ocean, especially at near-IR wavelength, resulting in a larger TOA reflectance for the same cloud optical depth. The average reflectance of land, ocean, and green vegetation has a similar wavelength dependence feature for three cases.

Now, we examine $1-\bar{I}_{norm,j}$ (**Figures 8b1–b3**), and $\frac{n_j}{N}$ (**Figures 8c1–c3**). We found that both $1-\bar{I}_{norm,j}$ and $\frac{n_j}{N}$ slightly depend on wavelength. In fact, $\frac{n_j}{N}$ for each reflector would be the same for all 10-wavelength images if they were taken concurrently. In reality, each of the 10-wavelength set of

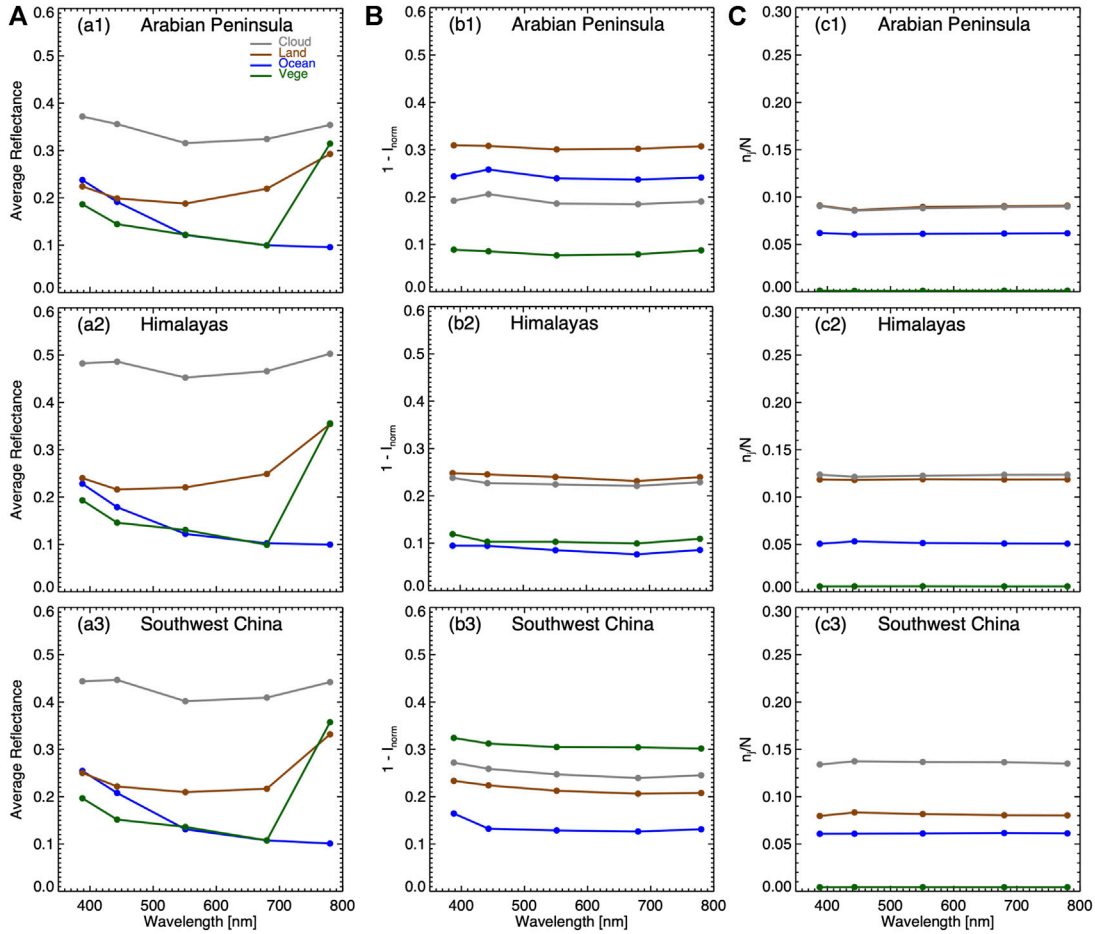

FIGURE 8 | (a1–a3) the average reflectance; **(b1–b3)** $1 - \bar{I}_{norm,j}$; **(c1–c3)** $\frac{n_j}{N}$ (the ratio of number of pixels in the Moon's shadow to total number of pixels in the EPIC image) for each reflector j in the penumbra for the three cases during the 2020 solar eclipse.

EPIC images is obtained at slightly different times and the Moon's shadow moves a little during the time intervals, resulting in a slightly different Moon's shadow and $\frac{n_j}{N}$ from one wavelength image to another. For randomly distributed reflector pixels in a complete circular Moon's shadow on the reference plane, we found that the average normalized solar irradiance ($\bar{I}_{norm,j}$) is almost independent of wavelength for the five EPIC wavelengths concerned. For the areas close to the umbra, the normalized irradiance for longer wavelength is larger than that for shorter wavelength; farther from the umbra, the normalized irradiance for longer wavelength is smaller than that for shorter wavelength (**Figure 4**); and, averaging over the whole penumbra yields similar $\bar{I}_{norm,j}$ for each wavelength. In reality, the pixel for a given reflector is not randomly distributed in the penumbra, resulting in a slight wavelength dependence in $\bar{I}_{norm,j}$.

For the Arabian Peninsula case, the factor of (**Figure 8b1**) is the largest for land followed by ocean, cloud, and green vegetation, respectively. The average normalized solar irradiance is about 0.69, 0.77, 0.81, and 0.92 for land, ocean, cloud, and green vegetation, respectively. Since the normalized solar irradiance monotonically increases with the distance from the center of the Moon's shadow (see **Figure 4**), the smaller normalized solar irradiance corresponds to a closer distance from a reflector to the center of the Moon's shadow. Thus, on average, land pixels, including desert and bare soil, are closest to the center of the Moon's shadow followed by ocean, cloud, and green vegetation. In addition to the average solar irradiance, the number of pixels determines the collective contribution from each individual reflector type. **Figure 8c1** shows that the ratio ($\frac{n_j}{N}$) is about 0.09, 0.09, 0.06, and 0.001 for land, cloud, ocean, and green vegetation, respectively. Multiplying $1 - \bar{I}_{norm,j}$ by $\frac{n_j}{N}$ yields the contribution factor. As a result, the contribution factor (η_j) is the largest for land (~0.027) followed by cloud (~0.017), ocean (~0.015), and green vegetation (~0.0001). Therefore, the reflectance reduction of each reflector can be explained by the average reflectance, the average distance to the center of Moon's shadow plus the area coverage of the reflector in the Moon's shadow.

Indeed, from **Figure 1**, one could visualize the area size of each reflector and the average distance to the center of the Moon's shadow for the 21 June 2020 eclipse. For the Arabian Peninsula

case, the Arabian Desert in the Arabian Peninsula, the Sahara Desert in Northern Africa, and the Ogaden Desert in Eastern Africa occupy the largest areas close to the center of the Moon's shadow. The Red Sea, the Persian Gulf, the Gulf of Oman, and the Arabian Sea are close to the center of the Moon's shadow; however, those areas are much smaller than the deserts. The clear area of the Indian Ocean is large, but farther from the center of the Moon's shadow. As a result, the average radial distance for land pixels to the center of the Moon's shadow is smaller (smaller $\bar{I}_{norm,j}$ or larger $1-\bar{I}_{norm,j}$) than clear ocean. Although some clouds are close to the center of the Moon's shadow in the Sudanian savanna, the Gulf of Oman, and the Arabian Sea, more clouds are farther away over the Indian Ocean, India, Southwest China, and Europe, resulting in a larger average radial distance for cloudy pixels to the center of the Moon's shadow (larger $\bar{I}_{norm,j}$ or smaller $1-\bar{I}_{norm,j}$) compared to clear land and clear ocean. The fractional coverage of green vegetation is small and contributes a little to the disk average reflectance (Wen et al., 2019). In this case, a small area of green vegetation coverage in Europe is visible and the green vegetation region is farther away from the center of the Moon's shadow with negligible area compared to land, ocean, and cloud (**Figure 8c1**).

For the Himalayas case (**Figures 8b2,c2**), the similar values of the factor $1-\bar{I}_{norm,j}$ (~0.23) and $\frac{n_j}{N}$ (~0.12) for land and cloud, indicates similar average distance to the center of the Moon's shadow and area coverage of the two reflectors, which can be seen in **Figure 1**. To the east and southeast of the center of the Moon's shadow, it is mostly cloudy; to the west and northwest of the center of Moon's shadow, it is mostly clear, resulting in similar average radial distance and area in the penumbra. The green vegetation in Europe and clear oceans (the Indian Ocean and the Pacific Ocean) are rather far away compared to land and cloud reflectors, resulting in a smaller and similar value of $1-\bar{I}_{norm,j}$ (~0.1) for both green vegetation and clear ocean. The area of green vegetation is evidently smaller than clear ocean; and $\frac{n_j}{N}$ is ~0.006 and ~0.05 for green vegetation and ocean, respectively. The contribution factor (η_j) is ~0.028 for both land and cloud, ~0.005 for ocean, and ~0.0006 for green vegetation, respectively. Again, the reflectance reduction of each reflector can be explained as the result of the brightness, the average distance from the center of Moon's shadow, and the area coverage of the reflector in the Moon's shadow.

For the Southwest China case (**Figures 8b3, c3**), the factor $1-\bar{I}_{norm,j}$ is the largest for green vegetation followed by cloud, land, and ocean, respectively; $\frac{n_j}{N}$ is the largest for cloud followed by land, ocean, and green vegetation respectively. The largest factor ($1-\bar{I}_{norm,j}$) of about 0.3 is for vegetation, which is mainly associated with green vegetation pixels in Mainland Southeast Asia or Indochinese Peninsula, including Cambodia, Laos, Myanmar, Vietnam, and China's Hainan Island. On average, those green vegetation pixels are much closer to the center of the Moon's shadow compared to cloud, land, and ocean although the area coverage of green vegetation is smallest with $\frac{n_j}{N}$ about 0.004 more than one order smaller than other reflectors. The second largest factor ($1-\bar{I}_{norm,j}$) of about 0.25 is for cloud, mainly due to large bright clouds to the east and north and broken clouds to the south and west of the umbra (see **Figure 1**). In fact, the area coverage of cloud with $\frac{n_j}{N}$ about 0.14 is the largest among the four reflectors. The third largest factor ($1-\bar{I}_{norm,j}$) of about 0.22 is for land. The area coverage with $\frac{n_j}{N}$ about 0.08 ranks second. On average, clear ocean pixels are farthest among all four reflectors and fractional coverage with $\frac{n_j}{N}$ about 0.06 smaller than that for clouds.

The contribution factor (η_j) is ~0.035 for cloud, 0.018 for land, ~0.008 for ocean, and ~0.001 for green vegetation, respectively. Thus, clouds contribute the most to the average reflectance reduction followed by land and ocean. With the larger contribution factor for green vegetation compared to both the Arabian Peninsula and Himalayas cases, the reflectance reduction from green vegetation is noticeable (**Figure 7C**), particularly for the near-IR wavelength at 780 nm, at which green vegetation is extremely reflective (see **Figure 6**, **Figure 8a3**).

It is important to note that the reflectance reduction for Arabian Peninsula case is significantly smaller compared to the Himalayas and Southwest China cases, mainly because part of the Moon's shadow falls outside of the Earth's disk. The Moon's shadow covers about 24% of the whole Earth disk, but a significant portion of the shadow falls outside of the Earth's disk, compared to ~28–30% for Himalayas and Southwest China cases (**Table 2**).

For the two cases of the 2017 eclipse (**Figure 9**), the average reflectance reductions are similar except for a decrease from 551 to 680 nm and a larger increase from 680 to 780 nm in reflectance reduction for the Columbia, Missouri case compared to the Casper, Wyoming case. Clouds contribute about 60 and 50% to the global spectral reflectance reduction, depending on wavelength, for the Casper and Columbia case, respectively. Clear land contributes about 30% to the global spectral reflectance reduction depending on wavelength for both cases. Clear ocean contribution for the Columbia case is larger than that for the Casper case since most clear ocean area is in the Atlantic Ocean to the east of the totality of the two eclipses (**Figure 1**). With the clear Atlantic Ocean areas are closer to Columbia than Casper, the contribution from clear ocean to the total reflectance reduction for the Columbia case is larger than Casper. Green vegetation makes a similar contribution to the reflectance for the two cases and a significant contribution to the disk reflectance reduction for the 2017 eclipse compared to the 2020 eclipse.

As demonstrated in the 2020 eclipse, the reduction of spectral reflectance of each reflector for the 2017 eclipse is proportional to the average spectral reflectance in the Moon's shadow (**Figures 10a1,a2**). The proportionality factor, or the contribution factor, is the product of $1-\bar{I}_{norm,j}$ and $\frac{n_j}{N}$ for each reflector. $1-\bar{I}_{norm,j}$ is largest (~0.55) for green vegetation followed by land (~0.45) for both the Casper and Columbia cases, because of relatively small average pixel to the center of shadow distance compared to ocean and cloud (**Figures 10b1,b2**). For cloud, $1-\bar{I}_{norm,j}$ is ~0.22 and ~0.18 for the Casper and Columbia case, respectively, because the major stratocumulus cloud system off the California coast is closer to Casper, Wyoming than Columbia, Missouri. For ocean, $1-\bar{I}_{norm,j}$ is smaller for the Casper case (~0.12) than that for the Columbia case (~0.18); the major body of water, the Atlantic Ocean, is relatively closer to Columbia than Casper. This is consistent with the larger ocean coverage for the Columbia case than the Casper case (**Figures 10c1,c2**), i.e., $\frac{n_j}{N}$ for ocean

TABLE 2 | The average fraction of area covered by different reflectors in the whole EPIC image (η_j/N) and associated standard deviation for selected five wavelengths.

	Casper	Columbia	Arabian pen	Himalayas	SW China
Ocean	0.053 (2.e-3)	0.065 (3.e-3)	0.061 (6.e-4)	0.051 (1.e-3)	0.061 (3.e-4)
Land	0.056 (4.e-4)	0.056 (1.e-4)	0.090 (2.e-3)	0.119 (2.e-4)	0.081 (1.e-3)
Cloud	0.137 (1.e-3)	0.145 (1.e-3)	0.089 (2.e-3)	0.123 (1.e-3)	0.136 (1.e-3)
Vege	0.020 (5.e-5)	0.022 (4.e-5)	0.001 (9.e-5)	0.006 (4.e-5)	0.004 (5.e-5)
Total	0.267	0.289	0.241	0.299	0.282

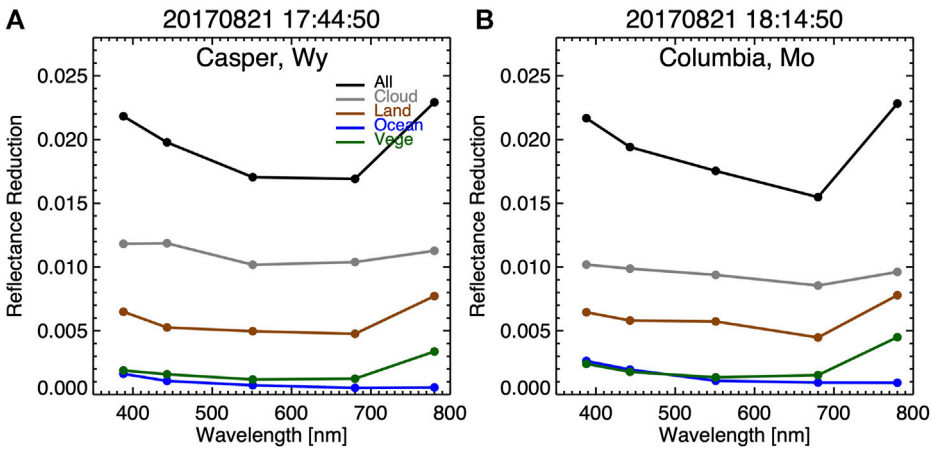

FIGURE 9 | Similar to **Figure 7** but the two cases during the 2017 solar eclipse.

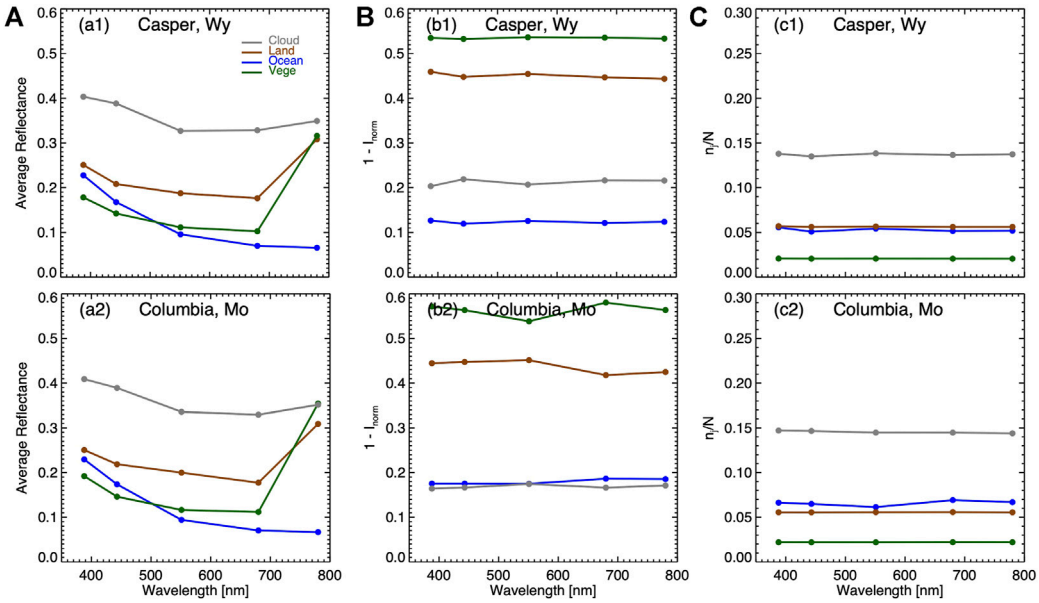

FIGURE 10 | Similar to **Figure 8** but for the two cases during the 2017 solar eclipse.

is ~0.007 for the Columbia case compared to ~0.005 for the Casper case. $\frac{n_j}{N}$ for cloud (~0.15), land (~0.05) and green vegetation (~0.02) is similar for the Casper and Columbia case, respectively. One can determine the contribution factor for each reflector for the two cases. For the Casper case, η_j is ~0.029 for cloud, 0.025 for land, ~0.011 for green vegetation, and ~0.007 for ocean, respectively. For the Columbia case, η_j is ~0.024 for cloud and land, ~0.012 for green vegetation and ocean,

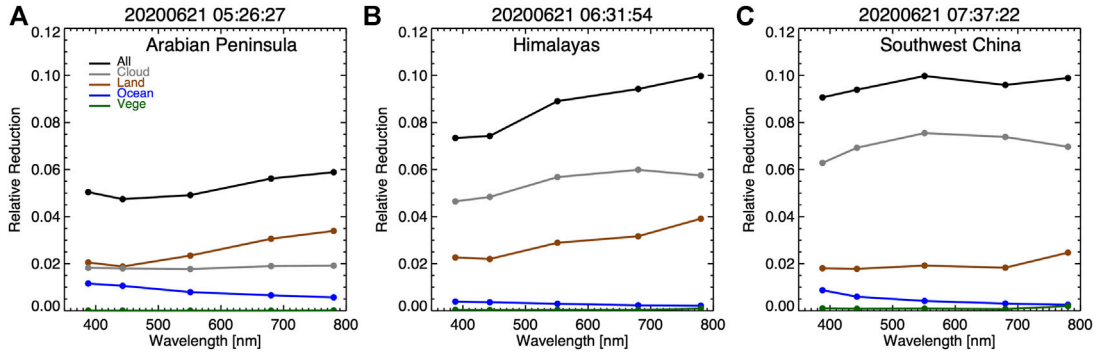

FIGURE 11 | Relative global average reflectance reduction with contributions from different reflector types for 2020 eclipse when the center of the Moon's shadow was in **(A)** Arabian Peninsula, **(B)** Himalayas, **(C)** Southwest China.

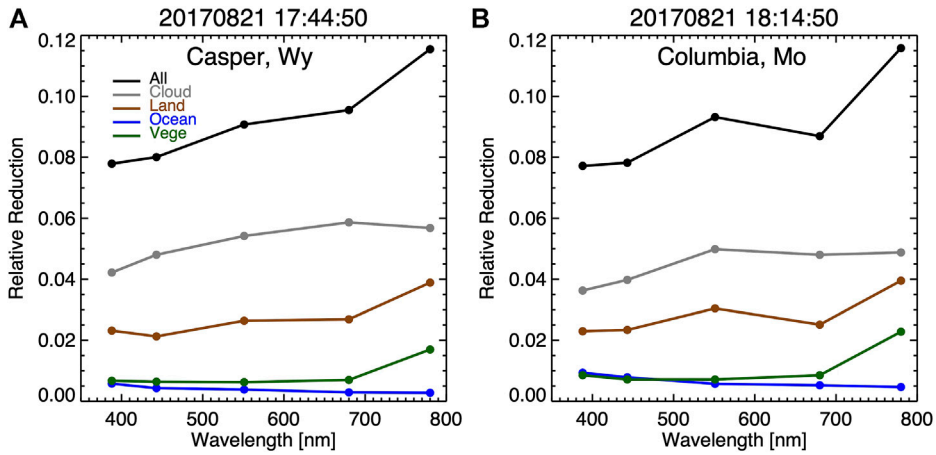

FIGURE 12 | Relative disk average reflectance reduction with contributions from different reflector types for 2017 eclipse when the center of the Moon's shadow was in **(A)** Casper, Wyoming, **(B)** Columbia, Missouri.

respectively. By combining the average reflectance and associated contribution factor, one obtains the average reflectance reduction.

The relative spectral reflectance reductions (defined as the difference between non-eclipse and eclipse reflectance divided by the eclipse reflectance) and associated components from different reflectors are presented in **Figure 11** and **Figure 12** for the 2020 and 2017 eclipse cases, respectively. For the Arabian Peninsula case, the average percent reflectance reduction increases with wavelength with an average of ~5.5%. The wavelength dependence of the percent reduction is mainly due to the increase of the reflectance from land compensated to some extent by the decrease of the reduction from clear ocean. For the Himalayas case, the average percent global reflectance reduction increases with wavelength with an average of ~9%. The wavelength dependence of the percent reduction is due to the increase of the reduction with wavelength from cloud and clear land. Green vegetation contributes little to the average relative reflectance reduction for both the Arabian Peninsula and Himalayas cases. For the Southwest China case, the reflectance reduction increases from 388 to 551 nm followed by a slight decrease from 551 to 680 nm and small increase to 780 nm. The wavelength dependence of the relative reduction can be explained by the contribution from each individual reflector. The total average reduction of ~9.5%, where cloud contributes over 7%, clear land contributes about 2%, and clear ocean contributes significantly at shorter wavelengths (~1% at 388 nm) and decreases toward longer wavelengths. The contribution from green vegetation is visible particularly at 780 nm wavelength.

For the 2017 eclipse, the wavelength dependence of the average reflectance reduction for the Casper case is similar to that for the Columbia case and can be explained by the contribution from each reflector (**Figure 12**). Similar to the absolute reductions, for the Casper case, cloud makes the larger contributions compared to the Columbia case; land makes similar percent reduction for the two cases; ocean and green vegetation contributes slightly more percentage reductions for the Columbia case compared to the Casper case. The total average reduction is ~9% for both cases.

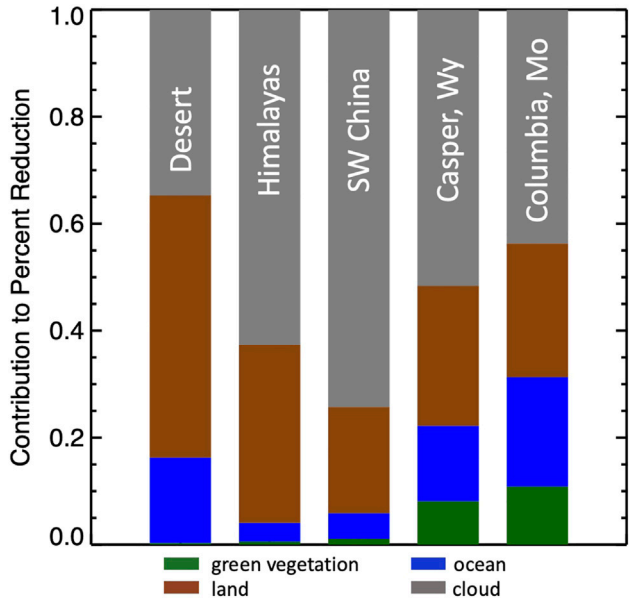

FIGURE 13 | Summary of percentage contribution from different reflectors for the three cases during 2020 solar eclipse and two cases during 2017 solar eclipse.

The contribution from each reflector type to the disk and spectrally averaged percent reflectance reduction is summarized in **Figure 13**. For 2020 solar eclipse over Arabian Peninsula, clear land (mostly desert) makes the largest contribution to the reduction, followed by clouds and clear ocean. For both the Himalayas and Southwest China cases, clouds contribute the most to the reduction, followed by clear land and clear ocean. Green vegetation makes little contribution to the reflectance reduction. For 2017 solar eclipse, clouds make the largest contribution to the total reduction, followed by clear land, clear ocean, and green vegetation.

SUMMARY AND DISCUSSION

We have analysed EPIC images to quantify and understand eclipse-induced disk spectral reflectance reduction. Radiative transfer calculations showed that different reflector types of the Earth have different spectral reflectance that affects the amount of eclipse radiances at TOA. The global reflectance reduction is the sum of the contribution from different reflectors. We showed that the reduction from each reflector is proportional to the average reflectance, the area coverage in the penumbra, and the average distance from the center of the Moon's shadow.

Using calculated reduced brightness during eclipses, we recovered the EPIC images under hypothetical non-eclipse conditions from eclipse images. We further classified dominant reflector types based on the recovered non-eclipse images. We found that the average spectral reflectance reductions for the three cases during the 2020 eclipse differ significantly from each other and two cases during 2017 eclipse. The differences were explained by the difference in the brightness of underlying reflectors, the associated radial distances to the center of the Moon's shadow as well as the area coverages in the Moon's shadow.

We also quantified the percentage reductions. For the 2020 eclipse, the spectrally averaged relative reflectance reduction is ~5.5%, ~9%, and ~9.5% for the Arabian Desert, Himalayas, Southwest China case, respectively, compared to ~9% for the two cases for 2017 eclipse. The reflectance reductions from different reflectors were used to interpret the disk average spectral reflectance reduction.

Note that the global reflectance reduction for the Arabian Peninsula case is about 5%, significantly smaller than the other cases. This difference is mainly due to a large portion of the Moon's shadow being outside of the Earth. Another factor is that desert is almost cloud-free and bright clouds farther away from the center of the Moon's shadow do not contribute effectively to the average reflectance reduction compared to the other cases.

DATA AVAILABILITY STATEMENT

Publicly available datasets were analyzed in this study. This data can be found here: https://search.earthdata.nasa.gov/.

AUTHOR CONTRIBUTIONS

GW composed the majority of this manuscript with assistance from AM, JH, and DW. GW performed most of the analyses with the help from AM. This is a follow-up paper of our earlier work led by JH (Herman et al., 2018a).

FUNDING

The DSCOVR EPIC project is funded by NASA Earth Science Division. GW and JH research was supported by the DSCOVR Science Management Project.

ACKNOWLEDGMENTS

AM acknowledges support from the NASA's DSCOVR Project. DW acknowledges support from the NASA's TSIS Project.

REFERENCES

Bernhard, G., and Petkov, B. (2019). Measurements of Spectral Irradiance during the Solar Eclipse of 21 August 2017: Reassessment of the Effect of Solar Limb Darkening and of Changes in Total Ozone. *Atmos. Chem. Phys.* 19, 4703–4719. doi:10.5194/acp-19-4703-2019

Blank, K., Huang, L.-K., Herman, J., and Marshak, A. A. (2021). Earth Polychromatic Imaging Camera Geolocation; Strategies to Reduce Uncertainty. *Front. Remote Sens.* 2, 715296. doi:10.3389/frsen.2021.715296

Calamas, D. M., Nutter, C., and Guajardo, D. N. (2018). Effect of 21 August 2017 Solar Eclipse on Surface-Level Irradiance and Ambient Temperature. *Int. J. Energ. Environ. Eng.* 10, 147–165. doi:10.1007/s40095-018-0290-8

Doelling, D., Haney, C., Bhatt, R., Scarino, B., and Gopalan, A. (2019). The Inter-calibration of the DSCOVR EPIC Imager with Aqua-MODIS and NPP-VIIRS. *Remote Sens.* 11, 1609. doi:10.3390/rs11131609

Emde, C., and Mayer, B. (2007). Simulation of Solar Radiation during a Total Eclipse: a challenge for Radiative Transfer. *Atmos. Chem. Phys.* 7, 2259–2270. doi:10.5194/acp-7-2259-2007

Eshelman, L. M., Tauc, M. J., Hashimoto, T., Gillis, K., Weiss, W., Stanley, B., et al. (2020). Digital All-Sky Polarization Imaging of the Total Solar Eclipse on 21 August 2017 in Rexburg, Idaho, USA. *Appl. Opt.* 59 (No. 21), F41–F52. doi:10.1364/AO/391736

Gedzelman, S. D. (2020). Solar Eclipse Skies and Limb Reddening. *Appl. Opt.* 59 (No. 21), F78–F84. doi:10.1364/AO.396964

Geogdzhaev, I. V., Marshak, A., and Alexandrov, M. (2021). Calibration of the DSCOVR EPIC Visible and NIR Channels Using Multiple LEO Radiometers. *Front. Remote Sens* 2. doi:10.3389/frsen.2021.671933

Geogdzhayev, I. V., and Marshak, A. (2018). Calibration of the DSCOVR EPIC Visible and NIR Channels Using MODIS Terra and Aqua Data and EPIC Lunar Observations. *Atmos. Meas. Tech.* 11, 359–368. doi:10.5194/amt-11-359-2018

Herman, J., Huang, L., McPeters, R., Ziemke, J., Cede, A., and Blank, K. (2018b). Synoptic Ozone, Cloud Reflectivity, and Erythemal Irradiance from Sunrise to sunset for the Whole Earth as Viewed by the DSCOVR Spacecraft from the Earth-Sun Lagrange 1 Orbit. *Atmos. Meas. Tech.* 11, 177–194. doi:10.5194/amt-11-177-2018

Herman, J., Wen, G., Marshak, A., Blank, K., Huang, L., Cede, A., et al. (2018a). Reduction in Earth Reflected Radiance during the Eclipse of 21 August 2017. *Atmos. Meas. Tech.* 11, 4373–4388. doi:10.5194/amt-11-4373-2018

King, M. D., Platnick, S., Menzel, W. P., Ackerman, S. A., and Hubanks, P. A. (2013). Spatial and Temporal Distribution of Clouds Observed by MODIS Onboard the Terra and Aqua Satellites. *IEEE Trans. Geosci. Remote Sens.* 51, 3826–3852. doi:10.1109/TGRS.2012.2227333

Koepke, P., Reuder, J., and Schween, J. (2001). Spectral Variation of the Solar Radiation during an Eclipse. *metz* 10, 179–186. doi:10.1127/0941-2948/2001/0010-0179

Madhavan, B. L., and Venkat Ratnam, M. (2021). Impact of a Solar Eclipse on Surface Radiation and Photovoltaic Energy. *Solar Energy* 223 (2021), 351–366. doi:10.1016/j.solener.2021.05.062

Marshak, A., Delgado-Bonal, A., and Knyazikhin, Y. (2021). The Effect of Scattering Angle on Earth Reflectance. *Front. Remote Sens.* 2. doi:10.3389/frsen.2021719610

Marshak, A., Herman, J., Adam, S., Karin, B., Carn, S., Cede, A., et al. (2018). Earth Observations from DSCOVR EPIC Instrument. *Bull. Amer. Meteorol. Soc. (Bams)* 99, 1829–1850. doi:10.1175/bams-d-17-0223.1

Mikhalev, A. V., Chernigovskaya, M. A., Beletsky, A. B., Kazimirovsky, E. S., and Pirog, O. M. (1999). Variations of the Ground-Measured Solar Ultraviolet Radiation during the Solar Eclipse on March 9, 1997. *Adv. Space Res.* 24 (5), 657–660. doi:10.1016/s0273-1177(99)00209-4

Neckel, H. (2005). Analytical Reference Functions F(λ) for the Sun's Limb Darkening and its Absolute Continuum Intensities (λ 300 to 1100 Nm). *Sol. Phys.* 229, 13–33. doi:10.1007/s11207-005-4081-z

Neckel, H., and Labs, D. (1994). *Solar Limb Darkening 1986–1990 (Lambda 303–1099 nm)* 153, 1–2, 91–114. doi:10.1007/BF00712494

Ockenfuß, P., Emde, C., Mayer, B., and Bernhard, G. (2020). Accurate 3D Radiative Transfer Simulation of Spectral Solar Irradiance during the Total Solar Eclipse of August 21, 2017. *Atmos. Chem. Phys.* 20, 1961–1976. doi:10.5194/acp-20-1961-2020

Ricchiazzi, P., Yang, S., Gautier, C., and Sowle, D. (1998). SBDART: A Research and Teaching Software Tool for Plane-Parallel Radiative Transfer in the Earth's Atmosphere. *Bull. Amer. Meteorol. Soc.* 79 (10), 2101–2114. doi:10.1175/1520-0477(1998)079<2101:sarats>2.0.co;2

Samanta, A., Knyazikhin, Y., Xu, L., Dickinson, R. E., Fu, R., Costa, M. H., et al. (2012). Seasonal Changes in Leaf Area of Amazon Forests from Leaf flushing and Abscission. *J. Geophys. Res. Biogeosciences* 117 (G1). doi:10.1029/2011jg001818

Sarid, G., Twedt, K. A., and Xiong, X. (2021). "Terra MODIS Sees Solar Eclipses: Analysis of Reflective Solar Band Response at Multiple Radiance Levels," in Proceedings of the SPIE 11727, Algorithms, Technologies, and Applications for Multispectral and Hyperspectral imaging XXVII, online only, United States, April 12–16, 2021, 1172701. doi:10.1117/12.2586219

Sharp, W. E., Silverman, S. M., and Lloyd, J. W. (1971). Summary of Sky Brightness Measurements during Eclipses of the Sun. *Appl. Opt.* 10, 1207–1210. doi:10.1364/AO.10.001207

Shaw, G. E. (1978). Sky Radiance during a Total Solar Eclipse: a Theoretical Model. *Appl. Opt.* 17, 272–278. doi:10.1364/ao.17.000272

Song, W., Knyazikhin, Y., Wen, G., Marshak, A., Mõttus, M., Yan, G., et al. (2018). Implications of Whole-Disc DSCOVR EPIC Spectral Observations for Estimating Earth's Spectral Reflectivity Based on Low-Earth-Orbiting and Geostationary Observations. *Remote Sens.* 10, 1594. doi:10.3390/rs10101594

Trees, V., Wang, P., and Stammes, P. (2021). Restoring the Top-Of-Atmosphere Reflectance during Solar Eclipses: a Proof of Concept with the UV Absorbing Aerosol index Measured by TROPOMI. *Atmos. Chem. Phys.* 21, 8593–8614. doi:10.5194/acp-21-8593-2021

Wen, G., Marshak, A., Song, W., Knyazikhin, Y., Mõttus, M., and Wu, D. (2019). A Relationship between Blue and Near-IR Global Spectral Reflectance and the Response of Global Average Reflectance to Change in Cloud Cover Observed from EPIC. *Earth Space Sci.* 6, 1416–1429. doi:10.1029/2019ea000664

Wen, G., Marshak, A., Tsay, S.-C., Herman, J., Jeong, U., Abuhassan, N., et al. (2020). Changes in the Surface Broadband Shortwave Radiation Budget during the 2017 Eclipse. *Atmos. Chem. Phys.* 20, 10477–10491. doi:10.5194/acp-20-10477-2020

Zerefos, C. S., Bali, D. S., Meleti, C., Bais, A. F., Tourpali, K., Kourtidis, K., et al. (2000). Changes in Surface UV Solar Irradiance and Ozone over the Balkans during the Eclipse of August 11, 1999. *J. Geophys. Res.* 105 (26), 463473. doi:10.1016/S0273-1177(01)00279-4

Conflict of Interest: The authors declare that the research was conducted in the absence of any commercial or financial relationships that could be construed as a potential conflict of interest.

Publisher's Note: All claims expressed in this article are solely those of the authors and do not necessarily represent those of their affiliated organizations, or those of the publisher, the editors and the reviewers. Any product that may be evaluated in this article, or claim that may be made by its manufacturer, is not guaranteed or endorsed by the publisher.